INORGANIC CHEMISTRY

FRONTIERS

Accepted Manuscript

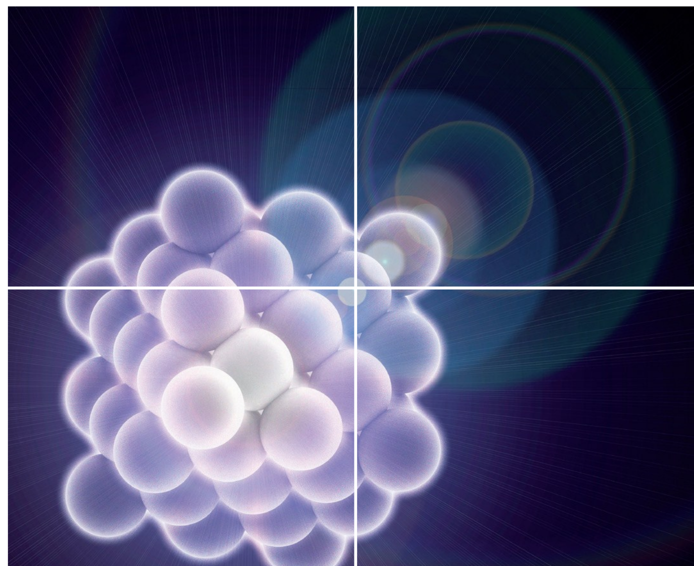

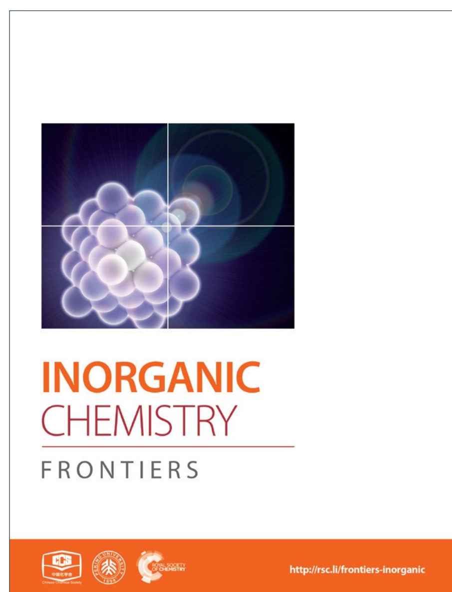

This is an *Accepted Manuscript*, which has been through the Royal Society of Chemistry peer review process and has been accepted for publication.

Accepted Manuscripts are published online shortly after acceptance, before technical editing, formatting and proof reading. Using this free service, authors can make their results available to the community, in citable form, before we publish the edited article. We will replace this *Accepted Manuscript* with the edited and formatted *Advance Article* as soon as it is available.

You can find more information about *Accepted Manuscripts* in the **Information for Authors**.

Please note that technical editing may introduce minor changes to the text and/or graphics, which may alter content. The journal's standard **Terms & Conditions** and the **Ethical guidelines** still apply. In no event shall the Royal Society of Chemistry be held responsible for any errors or omissions in this *Accepted Manuscript* or any consequences arising from the use of any information it contains.

中国化学会 Chinese Chemical Society

PEKING UNIVERSITY 1898

ROYAL SOCIETY OF CHEMISTRY

http://rsc.li/frontiers-inorganic

Lead-free tin chalcogenide thermoelectric materials

Min Zhou,[1,*] G. Jeffrey Snyder,[2,3] Laifeng Li,[1] Li-Dong Zhao[4,*]

[1]*Key Laboratory of Cryogenics, Technical Institute of Physics and Chemistry, Chinese Academy of Sciences, Beijing 100190, China*

[2]*Department of Materials Science and Engineering, Northwestern University, Evanston, Illinois 60208, United States.*

[3]*ITMO University, St. Petersburg, Russia*

[4]*School of Materials Science and Engineering, Beihang University, Beijing 100191, China.*

Abstract

Thermoelectric materials can be used to directly and reversibly convert waste heat into electrical power and have attracted significant attention. Lead-free tin chalcogenide (SnTe, SnSe, SnS) thermoelectric materials are recently regarded as promising thermoelectric materials due to the great progress in thermoelectric research field during the past several years. Analogous to PbTe, SnTe exists the simple high symmetry NaCl-type cubic structure and complex band structure, leading to capabilities of achieving high thermoelectric performance by band structure and microstructure engineering. SnSe/SnS are simple compounds, exhibits an intrinsically ultralow thermal conductivity, suggesting that a high thermoelectric performance also can be realized in simple layered, anisotropic and anharmonic systems, without nanostructuring. This short perspective summarizes the current strategies that could enhance the thermoelectric performance in bulk lead-free tin chalcogenides, such as band structure engineering, nanostructuring, and synergistically improved approaches. Future possible strategies for further enhancing thermoelectric performance in tin chalcogenides are also considered at the end of this perspective.

Keywords: thermoelectric materials; tin chalcogenide; band structure; microstructure

[*] Corresponding authors.
E-mail: mzhou@mail.ipc.ac.cn; zhaolidong@buaa.edu.cn

Inorganic Chemistry Frontiers Accepted Manuscript

1. Introduction

Thermoelectric materials have drawn vast attentions for centuries because thermoelectric effects can directly and reversibly convert heat into electrical power, thus providing an alternative for power generation and refrigeration. The conversion efficiency of thermoelectric technology is governed by the thermoelectric figure of merit (zT) defined as $zT = \alpha^2\sigma T/(\kappa_L+\kappa_e)$, where, α is the Seebeck coefficient, σ is the electrical conductivity, T is the absolute temperature,κ_e and κ_L are the electron thermal conductivity and lattice thermal conductivity (total thermal conductivity, $\kappa=\kappa_e+\kappa_L$), respectively. To maximize the thermoelectric figure of merit (zT) of a material, a large Seebeck coefficient, high electrical conductivity, and low thermal conductivity are needed. However, these parameters are determined by the inter-dependent relationships of the electronic structure and scattering of charge carriers (electrons or holes), and thus are not independently controllable. For metals or degenerate semiconductors (parabolic band, energy-independent scattering approximation[1]), the Seebeck coefficient is proportional to temperature and effective mass (m*), and inversely proportional to the charge carrier concentration (n), as seen in *eq.* (1). Thus, large Seebeck coefficient translates to large effective mass which is equivalent to large density-of-states (DOS) or flat bands at the Fermi level. High electrical conductivity requires a large mobility (μ) and large carrier (electrons or holes) concentration (n) through *eq.* (2). Therefore, high zT requires a combination of a large Seebeck coefficient (α) with a high electrical conductivity (σ). This is typically only achieved in heavily doped semiconductors combining high electron density-of-states (high effective masses) with high carrier concentrations, and high mobility[2] as seen in *eq.* (1) and (2).

For metals or degenerate semiconductors (parabolic band, energy-independent scattering approximation[1]) the Seebeck coefficient is given by:

$$\alpha = \frac{8\pi^2\kappa_B^2}{3eh^2} m^* T\left(\frac{\pi}{3n}\right)^{2/3} \quad (1)$$

where κ_B is the Boltzmann constant, m* is the density of states effective mass, h is the Planck constant, n is the carrier concentration, e is per electron charge.

Inorganic Chemistry Frontiers Accepted Manuscript

The electrical conductivity (σ) is related to n through the carrier mobility μ:

$$\sigma = ne\mu \quad (2)$$

On the other hand, thermal conductivity (κ) can be separated into two parts: the lattice or phonon contribution (κ_L) and the electronic contribution (κ_e), which is proportional to the electrical conductivity through the Wiedemann–Franz law[3]:

$$\kappa = \kappa_e + \kappa_L \quad (3)$$

$$\kappa_e = L\sigma T = ne\mu LT \quad (4)$$

Where L is the Lorenz number, κ is the total thermal conductivity. The Lorenz number can vary particularly with carrier concentration and can be reduced by as much as 20% from the free-electron value in low-carrier-concentration materials[1]. Thus in addition to optimizing the electronic transport properties, the lattice thermal conductivity must also be low. A variety of strategies such as nanostructuring[1, 4-9], seeking lattice anharmonicity[10, 11]and liquid-like behavior phonons[12], are proposed to obtain a low lattice thermal conductivity.

Good thermoelectric materials are therefore crystalline materials of "phonon glass-electron crystal"[2]. The electron-crystal requirement stems from the fact that crystalline semiconductors have been the best at meeting the compromises required from the electronic properties (Seebeck coefficient and electrical conductivity). The phonon-glass requirement stems from the need for as low a lattice thermal conductivity as possible. Over past decades, the research of bulk thermoelectric materials has made a great progress by diverse strategies (for example, band structure engineering, phonon engineering and seeking new promising thermoelectric system)[4, 5, 13-20] and the figure of merit (zT) reached even higher than 2.

Thermoelectric materials that used in the mid-temperature (500-1000 K) power generation are particularly attractive because most of the waste heat in industry and automobile exhaust is within this range[21, 22]. To date, the leading materials include the lead chalcogenides[4, 13, 23-27], filled skutterudites[28-32], half-Heusler compounds[33-36] , etc. In recent years, tin chalcogenides attracted increasing interests due to their greatly enhanced thermoelectric performance by band engineering and/or naonostructure[15, 18, 37-43], and lattice anharmonicity[15, 44].

Inorganic Chemistry Frontiers Accepted Manuscript

Skutterudites are a highly promising and deeply researched class of compounds. Since the void-filling atoms in skutterudites can act as electron donors or acceptors, partially filling the void space of skutterudites could lead to an optimum electron concentration. At the same time, these atoms can also act as strong phonon-scattering centers to greatly reduce the lattice thermal conductivity. Recently, broad-ranged investigations have been carried out on skutterudites with respect to the in-depth study of the physical process theory and the discovery of novel filled compounds. The thermoelectric performance of these materials has been greatly increased by both doping/filling[45-48] and nanostructure/nanocomposites strategies[31, 49-57]. On the basis of the "rattling" concept, the thermal conductivity was significantly reduced by single-, double-, triple-, and multiple-filling of elements into voids of the skutterudite structure, resulting in an improvement of zT values[58-60]. A high zT of 1.8 was reported in quadruple filled n-type skutterudites $(Sr, Ba, Yb, In)_yCo_4Sb_{12}$ at 823 K. In porous (Ba,In) double-filled skutterudite materials a maximum zT of 1.36 was obtained, in which the Seebeck coefficient was increased due to the electron filtering effect induced by nanostructures in the surfaces of pores and the lattice thermal conductivity was dramatically suppressed due to the enhanced pore-edge boundary scattering of long-wavelength phonons[51]. Besides, the compaction technique, hot press together with high-pressure torsion (HPT), is a new way to reduce the thermal conductivity (up to 40%) of skutterudites due to the additionally introduced defects[61, 62]. The zT value could be further enhanced to 1.9 at 835 K for $Sr_{0.09}Ba_{0.11}Yb_{0.05}Co_4Sb_{12}$ after severe plastic deformation via high-pressure torsion[62]. Thermoelectric properties of semiconductors are intimately related to their electronic band structure, which can be engineered via chemical doping[63, 64]. A high zT value of 1.3 was reported in $Yb_xCo_4Sb_{12}$ at 850 K due mainly to the band convergence of the light conduction band with the heavy conduction[65].

Another class of potential thermoelectric compounds is the half-Heusler compounds. The most attractive feature of half-Heusler alloys as promising thermoelectric materials is the large Seebeck coefficient (approximately 100 μVK^{-1} at room-temperature) and high electrical conductivities (1000–10000 S cm^{-1})[34, 66].

Inorganic Chemistry Frontiers Accepted Manuscript

However, on account of the relative high thermal conductivity, the *zT* values of the half-Heusler compounds are still much lower than those of the state-of-the-art thermoelectric materials. The thermoelectric properties were increased in isoelectronic-alloyed half-Heusler compounds through induced mass fluctuations and strain field effects[35, 66-68]. In recent year, half-Heusler compounds, such as MNiSn, MCoSb (M=Ti, Zr, Hf) and FeRSb (R=V, Nb), have gained popularity. Much work has been done in optimizing the electrical transport properties by tuning the carrier concentration[67-69] and suppressing the lattice thermal conductivity through alloying or nanostructuring[35, 66-68, 70-73]. A high *zT* of about 1.0 was reported for both n-type and p-type HH compounds[36, 67, 69, 70]. Further improvement of *zT* was realized in p-type $FeNb_{1-x}Hf_xSb$ heavy-band half-Heusler alloys due mainly to the enhanced point-defect and electron-phonon scatterings by high content of heavier Hf dopant. A high *zT* of 1.5 was reported at 1200 K[74].

Lead chalcogenides and their solid solutions are among the most efficient thermoelectric materials in the mid-temperature region. PbTe in particular, has a long history as thermoelectric materials and has been used for practical applications since the 1950s[75, 76]. Recently, the thermoelectric figure of merit (*zT*) of lead chalcogenides was continuously increased by synergistically using the concepts of band engineering (resonant levels[23, 24, 77], band convergence[13, 26, 78], bands alignment[5, 79, 80], etc.) and microstructure manipulation on all scaled hierarchical architectures[4, 5, 80-82]. A high *zT* value of 2.2 was reported for nanostructured $AgPb_mSbTe_{2+m}$ at 800 K in 2008[4]. In the past several years, the thermoelectric performance of the lead chalcogenides was enhanced and higher *zT* of 2.5 (923 K) was even reached for heavily alloyed PbTe-x%SrTe in 2016, in which significant band convergence boosting the power factors through non-equilibrium processing and endotaxial SrTe nanostructures greatly decreasing the lattice thermal conductivity[83]. However, the environmental concern regarding Pb in lead chalcogenides can frustrate their development and large-scale application.

In 2014, an outstanding high *zT* value of 2.6 at 923 K was reported in SnSe crystals[15], which have attracted a great interest in research on lead-free tin

Inorganic Chemistry Frontiers Accepted Manuscript

chalcogenides. In the past several years, the thermoelectric performance of tin chalcogenides (SnTe, SnSe, SnS) was greatly increased by band engineering and/or naonostructure[15, 18, 39-43, 84, 85]. High *zT* value of even 1.35-1.4 was reported in Hg-doped SnTe and In/Cd-codoped SnTe with CdS nanostructures[60]. These researches suggest that tin chalcogenides are attracting increasing attention as robust candidates of lead chalcogenides for thermoelectric power generation[15, 85-87]. It is worth noting that the local ferroelectric ordering was directly observed by piezo-response force microscopy (PFM) in SnTe above room temperature[88]. Then, Chang et. al. discovered the stable in-plane ferroelectricity in atomic-thick SnTe thin films, even down to a 1-unit cell (UC) limit[89]. These findings make SnTe an important member of the family of new multi-functional materials namely the ferroelectric-thermoelectrics. Table 1 lists *zT* peaks and corresponding temperature for some leading materials in the mid-temperature range (500-1000 K).

Table 1. *zT* peaks and corresponding temperature for some leading materials in the mid-temperature range (500-1000 K).

Materials system	Typical material	zT_{opt}	T_{opt}(K)
Lead chalcogenide	PbTe-x%SrTe[90]	2.5	923
Tin chalcogenide	SnSe[15]	2.6	923
Filled stutterudite	$(In, Sr, Ba, Yb)_yCo_4Sb_{12}$[60]	1.8	823K
	$Sr_{0.09}Ba_{0.11}Yb_{0.05}Co_4Sb_{12}$[62]	1.9	835K
Half-Heusler	$(Zr_{0.5}Hf_{0.5})_{0.5}Ti_{0.5}NiSn_{0.998}Sb_{0.002}$[91]	1.5	700

Our goal herein is to highlight the progress of promising tin chalcogenides (SnTe, SnSe and SnS) in recent years. It is not an exhaustive review, although lead chalcogenides are a significant part of thermoelectric research, they are beyond the scope of the current review. In this perspective, the recent advances in the field of tin chalcogenides (SnTe, SnSe and SnS) bulk alloys are summarized, e.g., band structure engineering strategies (resonant impurity doping and band convergence) lead to profound changes in the electrical properties. And nanostructuring/lattice anharmonicity strategies causes low lattice thermal conductivity. Future possible strategies for further enhancing thermoelectric performance in tin chalcogenides are

Inorganic Chemistry Frontiers Accepted Manuscript

also considered in this perspective.

2. SnTe and its solid solutions

Among tin chalcogenides (SnTe, SnSe and SnS), only SnTe exists in the rock salt crystal structure and shows isotropic thermoelectric properties. The stoichiometric SnTe is inherently riddled with Sn vacancies which normally results in a heavily doped (10^{20}~10^{21} cm^{-3}) p-type semiconductor[92-96]. Such high carrier concentration results in very high electrical conductivity (~7000 S cm^{-1} at room temperature), but extremely low Seebeck coefficient (corresponding to the minimum value of the Seebeck coefficient in the Pisarenko plot, as shown in Figure 1b) and high electrical thermal conductivity[92]. Therefore, SnTe did not receive extensive attentions due to its poor thermoelectric performance (a mediocre zT of about 0.5 at 900 K) in the past decades[92, 96]. Besides, a very small band gap (0.18 eV at room temperature) leads to a significant bipolar transport behavior, and a large energy offsets between the light valence band (L) and the heavy valence band (Σ) (ΔE, 0.3-0.4 eV at room temperature)[92-95] hinders the contribution of the heavier holes to the Seebeck coefficients (as shown in Figure 1a). It is therefore essential to modify the carrier concentration to more optimal levels with the aim of further enhancing the thermoelectric performance. Besides, recent studies unambiguously show that SnTe has a strong potential of being a good thermoelectric material through band structure engineering (band convergence, resonant doping, etc.) and/or nanostructure engineering[85-87, 97-100].

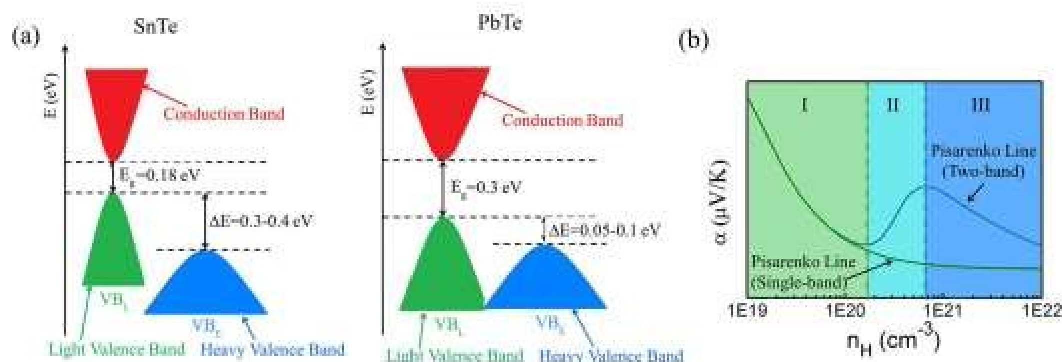

Fig. 1 (a) A schematic diagram of the near edge band structure in SnTe and PbTe. Both features two valence bands separated by an energy difference (ΔE) at room temperature. (b)The Seebeck coefficient as a function of Hall carrier concentration (Pisarenko relation) at 300 K. The SnTe

Inorganic Chemistry Frontiers Accepted Manuscript

compound has a smaller band gap (E_g, 0.18 eV) and larger energy offsets between the light valence band (VB_L) and the heavy valence band (VB_Σ) (ΔE, 0.3-0.4 eV) with respect to PbTe (E_g, 0.30 eV and ΔE, close to 0.1 eV at 300 K, respectively). Compared with the single band, the heavy valence band causes a Pisarenko line upturn. With increasing Hall carrier concentration the carrier transport of SnTe undergoes three regions, Region I (light valence band), region II (light valence band + partial heavy valence band), and region III (light valence band + heavy valence band)[99, 101, 102] (Reproduced with permission from J. Am. Chem. Soc., 138, 2366 (2016). Copyright 2016 American Chemical Society).

2.1 Carrier concentration optimizing

As mentioned above, SnTe is normally a highly degenerate p-type semiconductor with high carrier concentration (10^{20}-10^{21} cm^{-3}) ascribed to the intrinsic Sn deficiency, making it a poor thermoelectric material[96, 103]. To improve thermoelectric performance, it is necessary to either lower the carrier concentration to take advantage of the light L band or modify the band structures for better band convergence. It is found that bismuth, antimony, and Iodine are effective donors to reduce the hole concentration in SnTe[93, 95, 99]. On the other hand, Sn self-compensation is also an effective way of neutralizing the overly high hole concentration of SnTe[87]. Zhou et al. investigated the effects of both the donor- and acceptor-doping on the Hall carrier concentration and thermoelectric properties in SnTe[95]. It is found that donor-doping (Iodine) decreased the Hall carrier concentration, which enhanced the Seebeck coefficient and zT values utilizing the high mobility of the light band. Strikingly in contrast to the normal Pisarenko relationship based on the single parabolic band (SPB) model, acceptor-doping (extra Te or Gd) which increases the Hall carrier concentration also increases the Seebeck coefficient as well, due to the dominant contribution from heavy valence band. A two-band model (a Kane band for the light and a parabolic band for the heavy valence band) has been used to fit the experimental data of both the Seebeck coefficient and zT values. It is found that only one single maximum in zT as seen in most thermoelectric materials at higher temperatures although the Seebeck coefficient reached peak values at carrier concentration of $n_H \approx$ 4-6×10^{20} cm^{-3} (as shown in Figure 2). Experimentally, a maximum zT value of 0.6 (700 K) was obtained at $n_H \approx 4\times10^{19}$ cm^{-3} due to the solid solubility limit of Iodine in

Inorganic Chemistry Frontiers Accepted Manuscript

SnTe. Therefore, optimizing the SnTe carrier concentration towards the light band without obviously altering the host band structure is a valid approach to improve the thermoelectric properties of SnTe compound.

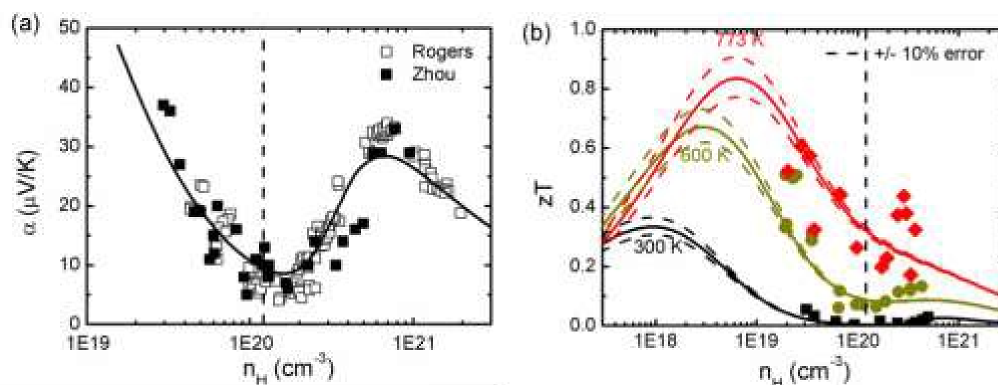

Fig. 2. (a) Seebeck coefficient, (b) zT as a function of Hall carrier concentration for donor-doped and acceptor-doped SnTe compounds. The black dashed vertical line in (a) and (b) corresponds to the un-doped SnTe ($n_H \approx 1.1\times10^{20}$ cm^{-3} at room temperature). The black open squares are Rogers' reported results[95]. The black solid squares, the dark yellow circles and the red diamonds are Zhou's reported results at 300 K, 600 K and 773 K, respectively[95]. The solid curves are the fitted zT values with the two-band model, and the dashed lines are the uncertainty values (Reproduced with permission from Phys. Chem. Chem. Phys., 16, 20741 (2014). Copyright 2014 Royal Society of Chemistry).

2.2 The band structure engineering

The complex band structure of SnTe leads to some strategies based on band structure engineering. The further enhancements of zT values are recently reported through DOS distortion (In doping)[86, 97] near room temperature and through valence band convergence (Cd, Hg, Mg, Ca and Mn alloying) individually[37, 43, 85, 87, 98, 100, 104, 105] above room temperature or simultaneously in a broad temperature range through In/Cd co-doping[97].

Figure 3a shows the schematic representations of the density of electron states (DOS) of the multiple valence bands and of the resonant states added to the host band. Compared with the host SnTe compound, the great enhancement of Seebeck coefficient is observed in In-doped SnTe (a resonant dopant in SnTe) at a given

Inorganic Chemistry Frontiers Accepted Manuscript

doping concentration where additional energy states were added to the host band [86, 97]. The calculation of the band structure of M-doped SnTe (M=Ga, In, Tl) confirmed that only In-doping introduces an obvious resonant state near the Fermi level. The resonant state was demonstrated to be from the anti-bonding of In-s and Te-p orbitals[106].

It is different from In-doped SnTe, the Seebeck coefficient of SnTe-based compounds without resonant dopants increases at higher carrier concentration (10^{20} cm^{-3}-10^{21} cm^{-3}) (as shown in Figure 3b), which can be attributed to the heavy valence band in SnTe[93, 95]. High Seebeck coefficient values of about 80 μV/K were obtained for In-doped SnTe at room temperature[86, 97], which is higher than that of the heavily doped SnTe[93]. However, the enhancement of the Seebeck coefficient diminishes with increasing temperature[86, 97]. This is similar to the Tl-doped PbTe system which only exhibits Seebeck coefficient enhancements at room temperature and below, but the effect weakens significantly above 500 K[24]. The synergistic combination of DOS distortion and nanostructure leads to a maximum *zT* of 1.1 at 873 K in In-doped SnTe[86] .

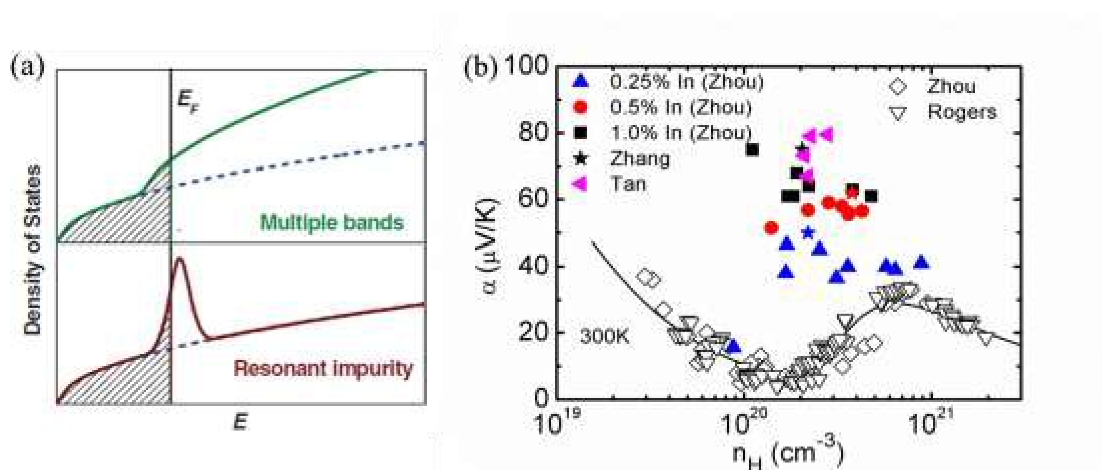

Fig. 3. (a) The schematic representation of the density of states of multiple bands and resonant impurity.[107] Both the resonant states and multiple bands increase the density of states and the Seebeck coefficient. (b) The enhancement of Seebeck coefficient at a similar Hall carrier concentration in SnTe-based compounds due to resonant doping (In) at room temperature. Solid symbols correspond to the data of In-doped SnTe with different In content. Open symbols correspond to the data without resonant dopants. Solid curve represents the results of the two-band model (Reproduced with permission from Adv. Mater., 24, 6125 (2012). Copyright 2012 John

Inorganic Chemistry Frontiers Accepted Manuscript

Wiley and Sons Inc).

Based on the enhanced Seebeck coefficient in In-doped SnTe, to achieve high thermoelectric performance over a broad temperature range, a careful control of the doping level and the position of the resonant levels is needed. This leads to studies of co-doped SnTe where the amount of resonant impurity (In) and extrinsic dopants (Iodine, Ag, extra Te) are adjusted independently. Figure 4 shows the composition dependences of the Hall carrier concentration and Seebeck coefficient in co-doped SnTe with In and additional impurities (Iodine, Ag, extra Te). Analogous to Tl-doped PbTe with additional Na impurity or excess Pb[108], the Hall carrier concentration (n_H) is stabilized over a broad range of additional impurities, which is called the stabilization region. From a simple chemistry point of view, in the presence of additional Te/Ag acceptors, the valence of some In atoms change from In^{1+} to In^{3+} compensating the free hole generated by extra Te/Ag. By contrast, In^{3+} changes to In^{+} with additional Iodine donors in SnTe compound. That is, in the stabilization region the In impurity suppressed extrinsic doping and stabilized (pinned) the Fermi level[109]. Similar to Tl resonant states in PbTe[108], the presence of two states (In^{+} and In^{3+}) per In atom provides an explanation for the amphoteric character of the given In impurity. Upon substituting additional co-dopants (I donors or extra Te/Ag acceptors) beyond the stabilization region, the Hall carrier concentration changed proportionally with additional impurity content (N_I, N_{Te}/N_{Ag}) (called doping region), indicating that the Fermi level is no longer pinned at the resonant level[110].

As shown in Figure 4b, higher Seebeck coefficients are found within the stabilization region, whereas it decreases when carrier density is either below or above it. This is a result of weakened influence from resonant levels as the Fermi level moves away. Also notice that Seebeck coefficients in samples with resonant levels are always higher than that without them given the same carrier density, which is due to the increased density of states (DOS) in SnTe with In impurities[110].

Inorganic Chemistry Frontiers Accepted Manuscript

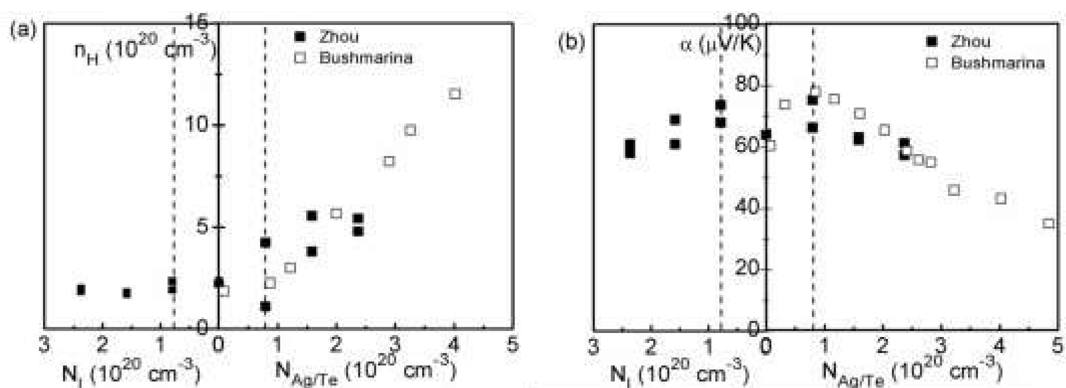

Fig. 4. (a) Hall carrier concentration, (b) Seebeck coefficient of co-doped $In_{0.01}Sn_{0.99}Te_{1-y}I_y$ (left side of the abscissa), $In_{0.01}Ag_zSn_{0.99-z}Te$/ $In_{0.01}Sn_{0.99}Te_{1+x}$ (right side of the abscissa) compounds at 300 K. The solid squares and open squares are Zhou's and Bushmarina's reported results, respectively[110].

As discussed above, the introduction of In in SnTe could create resonant levels inside the valence band, which enhances the Seebeck coefficient around room temperature[24, 77]. A similarly enhanced Seebeck coefficient at a given carrier concentration has also been found in $Sn_{1-x}M_xTe$ (M=Hg, Cd, Mn, Ca, Mg) due to a band convergence effect[37, 43, 85, 87, 100, 104] (as shown in Figure 5). Figure 5(a) shows the schematic energy diagram of the near edge band structure in SnTe and $Sn_{1-x}M_xTe$ (M=Hg, Cd, Mn, Ca, Mg). Compared with SnTe, M-doping (M=Hg, Cd, Mn, Ca, Mg) opens the band gap and diminishes the band offset between the light valence band and the heavy valence band (band convergence). The band gap enlargement also reduces the number of minority carriers at elevated temperature and suppresses the bipolar diffusion. The band offset reduction also results in the more efficient contribution of the heavy valence band to transport properties, enhancing the Seebeck coefficient, especially at high temperature. Tan et al. carried out density functional theory calculations of the electronic structures and confirmed the above modification of the band gap by Cd/Hg alloying[85, 87]. Similar band modifications have been found in Cd- and Mg-doped PbTe[26, 78] and PbSe[27]. From Figure 5(b), it is clear that the M-doped SnTe (M=Hg, Cd, Mn, Ca, Mg) compounds have much higher Seebeck coefficient than those without band convergence for similar hole concentration at room

Inorganic Chemistry Frontiers Accepted Manuscript

temperature. At high temperature, the increased valence band degeneracy also leads to an enhancement of the Seebeck coefficient because both valence bands are contributing efficiently to the transport properties.

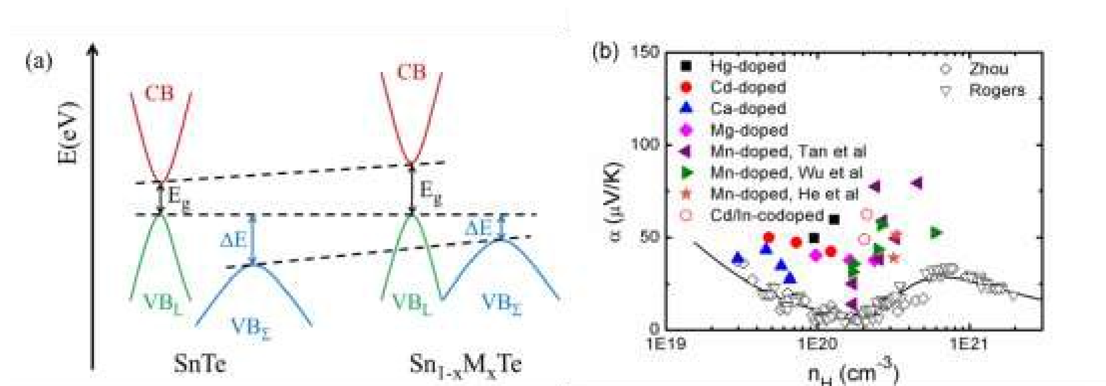

Fig. 5. (a) Schematic energy diagram of the near edge band structure in SnTe and $Sn_{1-x}M_xTe$ (M=Hg, Cd, Mn, Ca, Mg). E_g is the bandgap, ΔE is the band offset between the light valence band (VB_L) and the heavy valence band (VB_Σ). The relative positions of the conduction band (CB), the light valence band and the heavy valence band are shown for the undoped SnTe and doped $Sn_{1-x}M_xTe$ (M=Hg, Cd, Mn, Ca, Mg). (b) Seebeck coefficient as a function of Hall carrier concentration for $Sn_{1-x}M_xTe$ (M=Hg, Cd, Mn, Ca, Mg). The black squares, the red circles, the blue triangles and the magenta diamonds represent the results of Hg-doepd, Cd-doped, Ca-doped and Mg-doped SnTe. The purple left-triangles, the green right-triangles and the red stars present the results of Mn-doped SnTe. The red open circles are the results of the Cd/In-codoped SnTe. The open diamonds and downtriangles are doped SnTe without band convergence or resonant doping. Solid curves are the results of the two-band model.

It is worth noting that, Hg-doped SnTe has a lower lattice thermal conductivity compared to the Cd-doped SnTe[85]. This is mainly attributed to the larger atomic radius and mass difference between Hg and Sn which could cause stronger point defect scattering. A high maximum zT of 1.35 (900 K) and average zT_{ave} (300-900K) of 0.84 were reported for Hg-doped SnTe material[85].

The coexistence of resonant levels induced by In doping and band convergence enabled by Cd doping in SnTe produces a significant enhancement of the Seebeck coefficient and zT values over a broad temperature range[97]. As shown in Figure 6, the

Inorganic Chemistry Frontiers Accepted Manuscript

Seebeck coefficient of the In/Cd co-doped SnTe is significantly higher than that of the pristine SnTe at room temperature, which is very similar to In-doped SnTe[86, 97]. Moreover, these In/Cd co-doped samples have large Seebeck coefficients (~200 μV/K) at 923 K that are very close to those of Cd-doped ones (Figure 6a)[97]. These indicate that resonant levels introduced by the In dopant and band convergence caused by the Cd dopant may synergistically and harmoniously coexist in In and Cd codoped SnTe. First-principles density functional theory (DFT) calculations confirmed the coexistence of resonant levels and valence band convergence in In and Cd co-doped SnTe. The band offset (ΔE) between the light valence band and the heavy valence band decreases markedly to only 0.12 eV upon Cd-doping (as shown in the inset in Figure 6a). In and Cd co-doping yields an even lower ΔE of 0.04 eV[97]. It can therefore be concluded that band convergence still exists and plays a significant role in In/Cd co-doped SnTe. However, it is challenge to differentiate the two effects experimentally.

Combining the approaches of resonant levels and band convergence to modify the electronic structure of SnTe individually, one can readily improve both zT_{max} and zT_{ave} due to the broadening enhancement of Seebeck coefficients. As shown in Figure 6b, In-doping significantly increases zTs of SnTe in the low-temperature range, while, the zT values of the Cd-doped SnTe increase rapidly with increasing temperature. As a result, a maximum zT_{max} value of 1.1 (923 K) and average zT_{ave} of nearly 0.5 between 300 and 923 K were reported for In/Cd codoped SnTe[97].

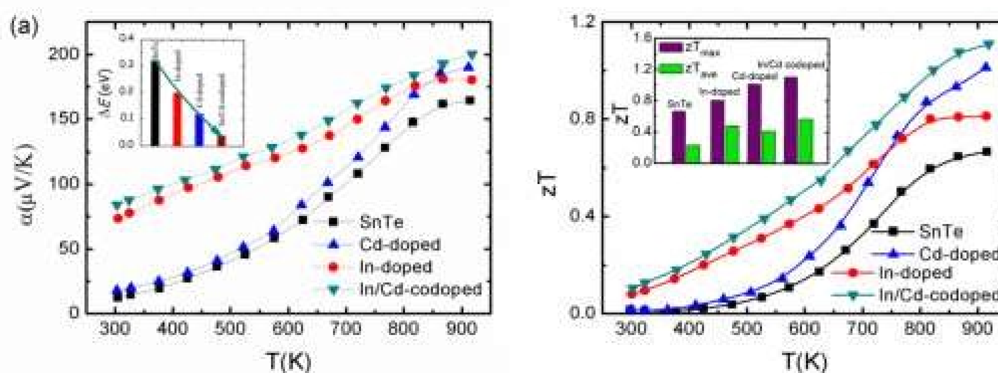

Fig. 6. Temperature dependence of (a) Seebeck coefficient, (b) zT values for the pristine SnTe, In-doped, Cd-doped and In/Cd-codoped SnTe. The inset in (a) is the band offset (ΔE) between the

Inorganic Chemistry Frontiers Accepted Manuscript

light valence band (VB_L) and the heavy valence band (VB_Σ) the pristine SnTe, In-doped, Cd-doped and In/Cd-codoped SnTe at room temperature. The inset in (b) shows the maximum zT values (zT_{max})and the average zT values (zT_{ave}) of the pristine SnTe, In-doped, Cd-doped and In/Cd-codoped SnTe.

2.3 Synergistically optimizing the electrical and thermal transport properties

The band engineering and carrier concentration optimization were reviewed to enhance the thermoelectric performance of SnTe, especially by modifying the electrical transport properties. Synergistic modification of electrical and thermal transport properties of SnTe can greatly increase zT values. Figure 7 shows the maximum zT values of nanostructured SnTe-based materials at 823 K[99], suggesting greatly enhanced zT values with endotaxial nanostructures (SrTe, CdS, etc).

The electrical transport properties of SnTe were optimized by tuning the carrier concentration to about 10^{19} cm^{-3} by using donor-doping (I, Bi, Sb, etc). The second phases (SrTe) were introduced into Bi-doped SnTe, forming effective strained endotaxial nanostructures to reduce the thermal conductivity. As a result, the lattice thermal conductivity decreases significantly from ~2.0 W m^{-1} K^{-1} in $Sn_{0.97}Bi_{0.03}Te$ to ~1.5 W m^{-1} K^{-1} in the $Sn_{0.97}Bi_{0.03}Te$ sample with 3.0% SrTe at room temperature and from ~1.1 to ~0.8 Wm^{-1} K^{-1} at 823 K. This leads to a zT value of 1.2 at 823 K for the $Sn_{0.97}Bi_{0.03}Te$ sample with 3.0% SrTe. This value is 33% higher than the zT value of 0.90 for the $Sn_{0.97}Bi_{0.03}Te$ sample without SrTe at 823K, indicating that the introduction of SrTe significantly boosts the thermoelectric properties of SnTe[99] (as shown in Figure 7). Tan et al. reported the thermoelectric performance of SnTe-$AgBiTe_2$ material[111]. Bismuth is an efficient electron donor in SnTe compound and reduced the hole concentration in SnTe. The Seebeck coefficient and electrical conductivity were enhanced. Similar to the $AgPb_mSbTe_{m+2}$ system (LAST), dispersed nanoscale precipitates formed and coherently distributed within the SnTe-$AgBiTe_2$ matrix. The distinctive nanostructures coupled with the point defect scattering by Ag and Bi alloying at Sn sites give rise to a very low lattice thermal conductivity of 0.7 W m^{-1} K^{-1} at 750 K. As a result, a high thermoelectric figure of merit zT of 1.1 at 775

Inorganic Chemistry Frontiers Accepted Manuscript

K is achieved.

As mentioned above, Cd-doping in SnTe modified the band structure, which enhanced the Seebeck coefficient and figure of merit to ~0.96 for $SnCd_{0.03}Te$[87]. The CdS/ZnS nanoscale precipitates were introduced into the matrix. These second phase precipitates exhibit three symmetry related variants with coherent or semi-coherent interfaces of well defined orientational relationship with the SnTe matrix. These exert little influence on the hole charge transport but are effective in scattering the phonons, suppressing the lattice thermal conductivity to a minimum value of 0.58 W m^{-1} K^{-1}. As a consequence, a high zT value of 1.3 was obtained for CdS-nanostructured SnTe at 873 K[87] (as shown in Figure 7).

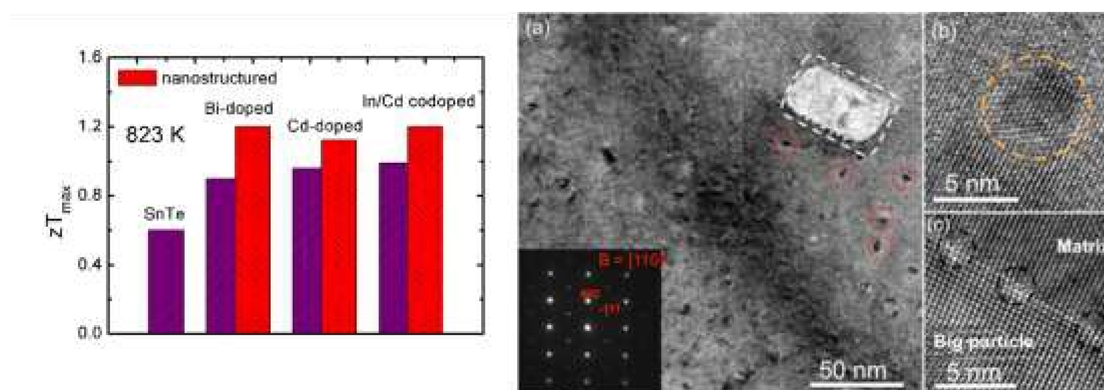

Fig. 7. The comparison of the maximum zT values for the SnTe-based compounds with and without nanostructures. The right photograph shows the electron microscopy of $Sn_{0.97}In_{0.015}Cd_{0.015}Te$-3%CdS with CdS nanoscale precipitates[97] (Reproduced with permission from J. Am. Chem. Soc., 137, 5100 (2015). Copyright 2015 American Chemical Society).

To reduce the lattice thermal conductivity of SnTe, all-scale hierarchical architectures, atomic-scale lattice distortions, nanoscale nanoprecipitates, and mesoscale grains boundaries can efficiently scatter wide spectrum of heat-carrying phonons, leading to significantly reduced lattice thermal conductivity. Figure 7 shows the microstructure of In/Cd co-doped SnTe with 3%CdS, which confirms the precipitates embedded in the matrix with coherent interfaces or semi-coherent interfaces[97]. As a consequence, a high zT_{max} of ~1.4 at ~923 K and a largely enhanced zT_{ave} of ~0.78 between 300 and 923 K are achieved in the SnTe system by

Inorganic Chemistry Frontiers Accepted Manuscript

In and Cd codoping and with hierarchical structuring[97].

Analogous to InSb-In_2Te_3 and GeTe-In_2Te_3 materials, the introduction of In_2Te_3 into SnTe compound not only creates resonant levels in the valence bands but also causes strong vacancy phonon scattering between the host Sn atoms and the guest structural vacancies of In_2Te_3, and additional interfacial scattering by In-rich nanostructures. As a result, a very low lattice thermal conductivity (κ_{lat}) of 0.6 W m^{-1} K^{-1} and a high zT value of 0.9 at 923 K for $(SnTe)_{3-3x}(In_2Te_3)_x$, which is about 50% improvement over the pristine SnTe[112]. Further carrier concentration optimization through Iodine substituting for Te leads to a peak zT of 1.1 at 923 K[112].

Analogous to lead chalcogenides [26, 27], alloying SnTe (E_g=0.18 eV) with larger band gap SnSe (E_g=0.83 eV) was expected to decrease the band offset (ΔE) between the light valence band (VB_L) and the heavy valence band (VB_Σ) bands, facilitating the band convergence and an improve Seebeck coefficient. Moreover, the thermal conductivity of SnTe may be further decreased by alloying with SnSe. As a result, the lattice thermal conductivity of the $SnTe_{1-x}Se_x$ was decreased. Resonance in the valence band through In doping along with the valence band convergence significantly improves the Seebeck coefficient in In-doped $In_ySn_{1-y}Te_{0.85}Se_{0.15}$, a peak zT of 0.8 was achieved in $SnTe_{1-x}Se_x$ system[113].

3. SnSe/S and their solid solutions

Unlike cubic SnTe, SnSe and SnS possess a layered orthorhombic crystal structure (space group *Pnma*) at room temperature, which can be derived from a three dimensional distortion of the NaCl structure[15, 114, 115]. As shown in Figure 8, there are two-atom-thick SnSe/S slabs (along the *b*-*c* plane) with strong Sn-Se/S bonding along the *a* direction. The structure contains highly distorted $SnSe_7$ or SnS_7 coordination polyhedra, which have three short and four very long Sn-Se/S bonds, and a lone pair of the Sn^{2+} sterically accommodated between the four long Sn-Se/S bonds. The two-atom-thick SnSe/S slabs are corrugated, creating a zig-zag accordion-like projection along the b axis. The easy cleavage in this system is along the (100) planes. At higher temperature (around 800 K for SnSe and 878 K for SnS), SnSe/S undergoes a second-order displacive phase transition to a five-fold coordinated *Cmcm* phase with a higher symmetry (Fig. 8d)[15, 115]. In the *Cmcm* phase, the atoms form double layers similar to those in the *Pnma* phase, but they are stacked along the *b* axis. Additionally,

Inorganic Chemistry Frontiers Accepted Manuscript

each atom is now coordinated to four neighbouring atoms at an equal distance in the *a*-*c* plane and one additional atom along the *b* axis. The anisotropy of the crystal structure is usually reflected in the thermal and electronic transport properties. Without exception, the electrical and thermal properties of SnSe/S are significantly different in the three crystallographic directions. The complex layered structure of SnSe contributes to the exceptionally low lattice thermal conductivity.

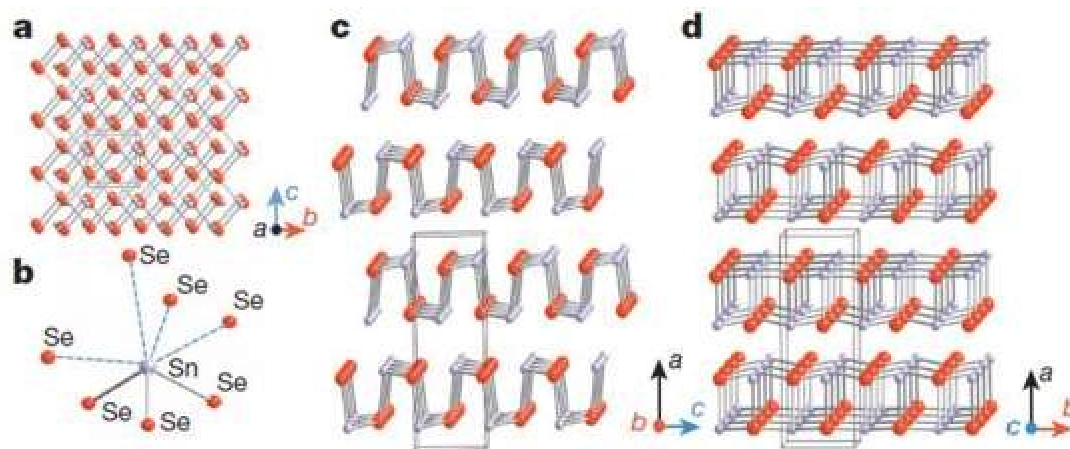

Fig. 8. Crystal structures of SnSe. (a) Crystal structure along the *a* axis: grey, Sn atoms; red, Se atoms. (b) Highly distorted $SnSe_7$ coordination polyhedron with three short and four long Sn-Se bonds. (c) Structure along the *b* axis. (d) Structure along the *c* axis[15] (Reproduced with permission from Nature,508, 373 (2014). Copyright 2014 Nature Publishing Group).

Shi et al. calculated the band structure of *Pnma*-SnSe and *Cmcm*-SnSe phases[116]. It is found that the band gap of *Pnma*-SnSe and *Cmcm*-SnSe is 0.829 eV and 0.464 eV, respectively. The calculated band gap (0.829 eV) is in agreement with optical-absorption measurements (0.86 eV[15] and 0.898 eV[117]). In comparison, the band gap is approximately 1.09 eV for the *Pnma*-SnS phase and 0.42 eV for the *Cmcm*-SnS phase[115]; these values agree with the previously reported theoretical and experimental results, which vary in the range of 1.07−1.11 eV in the *Pnma* phase and are equal to 0.1-0.3 eV in the *Cmcm* phase[118-122]. The significantly smaller band gap in the *Cmcm* phase will lead to increased bipolar conduction hindering performance at high temperatures.

Though SnSe is a well-known semiconductor studied for its potential in solar cells or in phase-change memory alloys[123, 124], SnSe/S compound was even historically ignored by the thermoelectric community due to its high electrical resistivity and low *zT* values (0.15 for SnSe, 0.28 for SnS at room temperature)[125]. Very recently, an

Inorganic Chemistry Frontiers Accepted Manuscript

investigation of the thermoelectric performance of single-crystalline tin selenide (SnSe) has revealed that this binary alloy shows extremely high *zT* values of 2.62 and 2.3 at 923K (i.e., in the high-temperature *Cmcm* phase) along the *b* and *c* axes, respectively (as shown in Figure 9). These outstanding and record values observed along the *b* and *c* directions arise due to a favorable combinations of high carrier mobility, large Seebeck coefficient and extremely low thermal conductivity values presumably due to a strong anharmonicity of the chemical bonding[15].

Very differently, the low temperature *Pnma* phase, however, shows much lower thermoelectric properties, which greatly limits applications of this material. Acceptor-doping (Na, Ag) in p-type SnSe single crystal increased the carrier concentration from 10^{17} cm^{-3} to 10^{19} cm^{-3} at room temperature[17]. The theoretical calculations show that the Fermi level is shifted upon Na-doping, the valence band edge is flattened, and the number of carrier pockets is enlarged. All three effects have a positive influence on the electronic transport properties of doped SnSe along the *b*-axis, the direction where the thermoelectric performance is maximized[17]. The overall effects contribute an excellent power factor and a high figure of merit, which extend over a broad range of temperatures. An average *zT* of 1.17 was reached over the temperature range of 300-800 K and the peak *zT* value is excess of 2 at 800 K in the case of $Sn_{0.97}Na_{0.03}Se$[17] (as shown in Figure 9).

Yet, the use of layered single crystals in thermoelectric devices is usually prevented by their poorer mechanical properties in comparision to polycrystalline materials and by the complex conditions (particularly when they are air sensitive) required to grow them. To date, most reports on SnSe are on polycrystalline samples because of the ease of preparing them compared to slow process of growing and cutting single crystals. It is therefore essential to determine the thermoelectric potential of polycrystalline materials.

It has so far proved difficult to translate high *zTs* in single crystals SnSe to polycrystalline samples because it is a challenge to obtain comparable electrical transport properties (especially for carrier mobility). The hole mobility of the single crystals is ~250 $cm^2V^{-1}s^{-1}$ (at the carrier density of about $3\times10^{17}cm^{-3}$)[15]. Given the strong 2D character of the SnSe structure specimen preparation can also lead to varying degrees of spatially averaged plate orientations and preferential orientation. For example, the carrier mobility along the *b* axis of SnSe single crystals is 10 times higher than the carrier mobility along the a axis[15]. Polycrystalline samples introduce

Inorganic Chemistry Frontiers Accepted Manuscript

Inorganic Chemistry Frontiers Accepted Manuscript

many grain boundaries which are good for reducing lattice thermal conductivity but also reduce mobility (less than 50 $cm^2V^{-1}s^{-1}$ at room temperature) and electronic conductivity[38]. This difference persists to high temperature. The hole mobility of polycrystalline SnSe is 10-15 $cm^2V^{-1}s^{-1}$ at 750K , which is only a fraction of the value ~50 $cm^2V^{-1}s^{-1}$ for the single crystals, resulting in much lower power factor and zT values[38]. The reduced mobility at higher temperature suggests the increased phonon-scattering by grain boundaries. This is in contrast to PbTe, PbSe and SnTe that show the mobility of dense, polycrystalline samples can be quite similar to single crystals[27, 95, 126-129].

In addition to the big different carrier mobility, the thermal conductivity is another issue that leads to the zT of SnSe crystals could not transfer to SnSe polycrystals. There is a spread of thermal conductivity values (even though all deal with polycrystalline SnSe samples) with some groups[130, 131], reporting extremely low thermal conductivity similar to or lower than single crystals SnSe while others reporting higher values[38, 132]. The thermal conductivity spread may result from the off-stoichiometry or surface oxidation[133]. SnSe after a week or month long exposure to air could result in some Sn oxidation[134], especially in porous polycrystalline samples. Surface oxidation in polycrystalline SnSe samples yields SnO_2 which itself has over about 140 times higher thermal conductivity of ~ 98 $Wm^{-1}K^{-1}$.[135]. Moreover, SnO_2 is humidity sensitive, thus results in some extra high thermal conductivity products[136, 137]. Sassi et al. studied the thermoelectric properties of the undoped SnSe. A maximum zT value of 0.5 was obtained at 823 K[132]. This value is significantly lower than those measured in single crystals by Zhao et al. due to higher thermal conductivity and electrical resistivity.

Chere, Leng and Wei et al. reported studies on the thermoelectric properties enhancement of SnSe polycrystals by optimizing the carrier concentration in polycrystalline Na-doped SnSe[40, 138, 139]. It is shown that Na doping effectively increase the carrier concentration from 10^{17} cm^{-3} for undoped SnSe to 10^{19} cm^{-3} for Na-doped SnSe. As a result, zT values of 0.8 was obtained along the hot pressing direction due to the low intrinsic thermal conductivity and enhanced power factor at an optimum Na doping of 1.5 atm%[40, 138] (as shown in Figure 9). Chen and Leng also reported analogous result for Ag-doped SnSe polycrystals[38, 140].

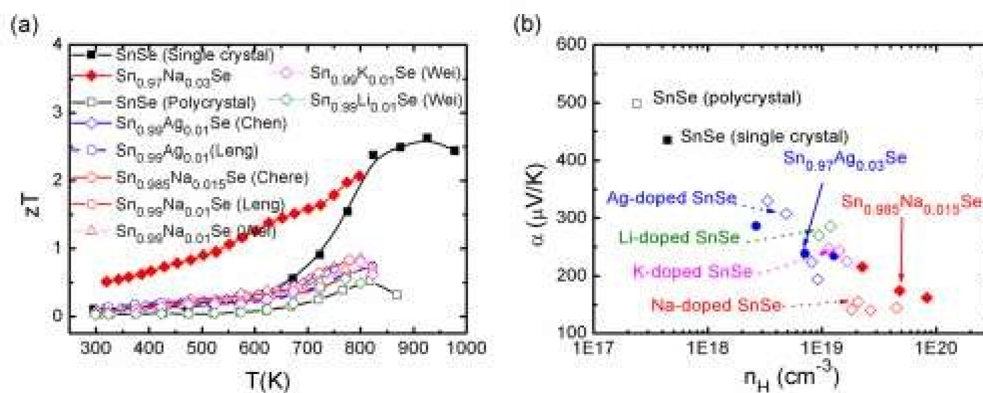

Fig. 9. (a) *zT* values of the prinstine SnSe and the Ag/alkali metals-doped SnSe single crystals and polycrystals, (b) Seebeck coefficient as a function of the Hall carrier concentration for the prinstine SnSe and the Ag/alkali metals-doped SnSe single crystals and polycrystals at room temperature. The solid marks show the data of SnSe-based single crystals, and the open marks show the data of SnSe-based polycrystals in both (a) and (b).

Zhang et. al. studied the thermoelectric properties of the Iodine-doped n-type SnSe polycrystalline by melting and hot pressing. A peak *zT* of about 0.8 was observed at about 773 K along the hot pressing direction. With increasing content of iodine, the carrier concentration changed from 2.3×10^{17} cm^{-3} (p-type) to 2.0×10^{17} cm^{-3} (n-type). By alloying with 10 at% SnS, even lower thermal conductivity and an enhanced Seebeck coefficient were achieved, leading to an increased *zT* of about 1.0 at about 773 K also along the hot pressing direction[141].

Highly textured polycrystalline SnSe exhibits high Hall mobility, leading to a higher power factor of over 9 $\mu W\ K^{-2}\ cm^{-1}$. This value is almost double of those reported polycrystalline SnSe. The enhancement of the electrical transport properties provides a good opportunity to improve the *zT* values of the polycrystalline SnSe. The maximum *zT* value of over 1 was reported at 873 K[142, 143].

It is very interesting that the SnSe transforms from a semiconducting to semi-metallic state under moderate pressure (12.6 GPa), followed by an orthorhombic to monoclinic structural transition. The average grain size of SnSe decreases significantly with increasing pressure. First-principles band structure calculations confirm the electronic transition, and reveal that the semimetal character of SnSe can be attributed to the enhanced coupling of Sn-5s, Sn-5p, and Se-3p states under compression, which results in the closure of the energy band gap[144]. The pressure

Inorganic Chemistry Frontiers Accepted Manuscript

modulates the electrical transport and microstructure, which may be an approach to improve the thermoelectric properties of SnSe.

SnS is attractive due to its inexpensive, nontoxic elements as well as its complex band structure[145]. Analogous to SnSe, the SnS shows anisotropic thermoelectric properties and exceptionally low lattice thermal conductivity due to the complex layered structure. It is significantly different from the case of SnSe, the undoped SnS has a large electrical resistivity (≥10 Ω cm)[146] due to the very low carrier concentration (about 10^{16} cm^{-3})[147, 148] and does not exhibit good thermoelectric performance even in the high-temperature *Cmcm* phase[115]. A maximum zT value of just 0.16 was reported at 823 K for the undoped SnS. Bera et al. performed a high-throughput first-principles study of extrinsic defects in SnS aimed at exploring the different p-dopants that could potentially enhance the carrier concentration in SnS. The study indicated that monovalent cations are potential doping candidates to optimize the fraction of itinerant holes in SnS[149]. Experimentally, Tan et al synthesized Ag-doped SnS compound by mechanical alloying and spark plasma sintering and systematically investigated the thermoelectric transport properties. The carrier concentrations increased to around $2.7\text{-}3.6\times10^{18}$ cm^{-3} at room temperature, in good agreement with the theoretical prediction[149]. Sun et al. present a detailed theoretical study of the p- and n-type doped thermoelectric properties of SnS across the *Pnma-Cmcm* phase transition. The study predicts that higher peak zT values will be obtained in the high-temperature *Cmcm* phase for both *p*- and *n*-type doped SnS at their optimized doping concentration (about 10^{19} cm^{-3})[115]. Han et. al. studied the thermoelectric properties of the SnSe-SnS solid solution. The results showed the complete solid solution of SnSe-SnS compounds. The band gap approximately linearly increased from 0.9 eV (SnSe) to 1.16 eV (SnS). A maximum zT of 0.82 was reported for $SnSe_{0.8}S_{0.2}$ in the direction parallel to the pressing direction[41]. Table 2 shows the thermoelectric properties of some leading tin chalcogenides and their solid solutions.

Inorganic Chemistry Frontiers Accepted Manuscript

Table 2 The thermoelectric properties of some leading tin chalcogenides (SnTe, SnSe, SnSe) and their solid solutions.

Materials system	**Single crystal/ Polycrystal**	**Typical compound**	zT_{opt}	T_{opt}(K)	n_{opt} (cm^{-3})
SnTe-based materials	Polycrystal	$Sn_{0.98}Bi_{0.02}Te$-x%HgTe[85]	1.35	910	2.2×10^{20}
SnSe-based materials	Single crystal	SnSe[15]	2.6	923	3.0×10^{17}
	Polycrystal	$SnSe_{1-x}I_x$-SnS[150]	1.0	773	2.0×10^{17}
SnS-based materials	Polycrystal	SnS-x%Ag[42]	0.6	923	2.8×10^{18}

4. Summary and outlook

Tin chalcogenides, a kind of IV-VI semiconductors, did not receive significant attention during the past decades due to their poor thermoelectric performance. However, the research of tin chalcogenides has made a great progress in the past several years.

Band engineering (resonant levels, band convergence, etc.) and/or nanostructuring contribute to the increased *zT* value in SnTe and its solid solutions. Disorder on multiple length scales, from point defects to crystal boundaries, can be used to scatter phonons of different frequencies. Besides, additional approaches will likely be indispensable for increasing the power factor to achieve further significant *zT* improvements.

On the other hand, the large Grüneisen parameter (reflecting the anharmonic and anisotropic bonding) contributes to the ultralow lattice thermal conductivity and the exceptional *zT* in SnSe compound, which highlights alternative strategies to nanostructuring for achieving high thermoelectric performance. The carrier concentration control (p-type doping) was used to enhance the power factor and *zT* values of the low-temperature phase SnSe. Band engineering, such as resonant states, is anticipated to enhance the electrical transport properties and the average *zT* values of the SnSe/S compounds.

The concepts of band engineering (resonant levels, band convergence, etc.) and microstructure manipulation on all scales have led to a stronger insight and understanding of the complex interrelationships among materials properties (thermal and electrical transport properties) and provided guiding principles in the optimization

Inorganic Chemistry Frontiers Accepted Manuscript

of existing thermoelectric materials and for designing new materials with potential applications. The environmental impact of the thermoelectric materials must be taken into account in the future applications.

Acknowledgment

The present work was supported by Key Laboratory of Cryogenics, TIPC, CAS under grant number CRYOQN201501. This work was also supported by the "Zhuoyue" program of Beihang University, the Recruitment Program for Young Professionals, NSFC under Grant No. 51571007, and the Fundamental Research Funds for the Central Universities (L.D.Z).

References

1. G. J. Snyder and E. S. Toberer, Nature Materials **7** (2), 105-114 (2008).
2. D. M. Rowe, *CRC handbook of thermoelectrics*. (CRC press, 1995).
3. M. Dresselhaus, in *Nobel Symposium 153: Nanoscale Energy Converters*, edited by H. Linke, M. Borgstrom, T. Pullerits, L. Samuelson, V. Sundstrom and O. Inganas (2013), Vol. 1519, pp. 36-39.
4. K. F. Hsu, S. Loo, F. Guo, W. Chen, J. S. Dyck, C. Uher, T. Hogan, E. Polychroniadis and M. G. Kanatzidis, Science **303** (5659), 818-821 (2004).
5. K. Biswas, J. Q. He, Q. C. Zhang, G. Y. Wang, C. Uher, V. P. Dravid and M. G. Kanatzidis, Nature Chemistry **3** (2), 160-166 (2011).
6. B. Poudel, Q. Hao, Y. Ma, Y. Lan, A. Minnich, B. Yu, X. Yan, D. Wang, A. Muto and D. Vashaee, Science **320** (5876), 634-638 (2008).
7. Y. Pei, J. Lensch-Falk, E. S. Toberer, D. L. Medlin and G. J. Snyder, Advanced Functional Materials **21** (2), 241-249 (2011).
8. S. Il Kim, K. H. Lee, H. A. Mun, H. S. Kim, S. W. Hwang, J. W. Roh, D. J. Yang, W. H. Shin, X. S. Li, Y. H. Lee, G. J. Snyder and S. W. Kim, Science **348** (6230), 109-114 (2015).
9. C. J. Vineis, A. Shakouri, A. Majumdar and M. G. Kanatzidis, Advanced Materials **22** (36), 3970-3980 (2010).
10. G. J. Tan, L. -D. Zhao, M. G. Kanatzidis, Chemical Reviews, 2016, doi: 10.1021/acs.chemrev.6b00255.
11. D. T. Morelli, V. Jovovic and J. P. Heremans, Physical Review Letters **101** (3) (2008).
12. H. L. Liu, X. Shi, F. F. Xu, L. L. Zhang, W. Q. Zhang, L. D. Chen, Q. Li, C. Uher, T. Day and G. J. Snyder, Nature Materials **11** (5), 422-425 (2012).
13. Y. Pei, X. Shi, A. LaLonde, H. Wang, L. Chen and G. J. Snyder, Nature **473** (7345), 66-69 (2011).
14. H. Liu, X. Yuan, P. Lu, X. Shi, F. Xu, Y. He, Y. Tang, S. Bai, W. Zhang, L. Chen, Y. Lin, L. Shi, H. Lin, X. Gao, X. Zhang, H. Chi and C. Uher, Advanced Materials **25** (45), 6607-6612 (2013).
15. L.-D. Zhao, S.-H. Lo, Y. Zhang, H. Sun, G. Tan, C. Uher, C. Wolverton, V. P. Dravid and M. G. Kanatzidis, Nature **508** (7496), 373-+ (2014).
16. B. Zhong, Y. Zhang, W. Li, Z. Chen, J. Cui, W. Li, Y. Xie, Q. Hao and Q. He, Applied Physics Letters **105** (12) (2014).

Inorganic Chemistry Frontiers Accepted Manuscript

17. K. Peng, X. Lu, H. Zhan, S. Hui, X. Tang, G. Wang, J. Dai, C. Uher, G. Wang and X. Zhou, Energy & Environmental Science **9** (2), 454-460 (2016).
18. L.-D. Zhao, G. Tan, S. Hao, J. He, Y. Pei, H. Chi, H. Wang, S. Gong, H. Xu, V. P. Dravid, C. Uher, G. J. Snyder, C. Wolverton and M. G. Kanatzidis, Science **351** (6269), 141-144 (2016).
19. Y. He, T. Day, T. Zhang, H. Liu, X. Shi, L. Chen and G. J. Snyder, Advanced Materials **26** (23), 3974-3978 (2014).
20. K. Tyagi, B. Gahtori, S. Bathula, S. Auluck and A. Dhar, Applied Physics Letters **105** (17) (2014).
21. C. T. Hsu, G. Y. Huang, H. S. Chu, B. Yu and D. J. Yao, Applied Energy **88** (4), 1291-1297 (2011).
22. C. Wu, Applied Thermal Engineering **16** (1), 63-69 (1996).
23. J. P. Heremans, V. Jovovic, E. S. Toberer, A. Saramat, K. Kurosaki, A. Charoenphakdee, S. Yamanaka and G. J. Snyder, Science **321** (5888), 554-557 (2008).
24. J. P. Heremans, B. Wiendlocha and A. M. Chamoire, Energy & Environmental Science **5** (2), 5510-5530 (2012).
25. Y. Pei, A. D. LaLonde, H. Wang and G. J. Snyder, Energy & Environmental Science **5** (7), 7963-7969 (2012).
26. L. D. Zhao, H. J. Wu, S. Q. Hao, C. I. Wu, X. Y. Zhou, K. Biswas, J. Q. He, T. P. Hogan, C. Uher, C. Wolverton, V. P. Dravid and M. G. Kanatzidis, Energy & Environmental Science **6** (11), 3346-3355 (2013).
27. H. Wang, Z. M. Gibbs, Y. Takagiwa and G. J. Snyder, Energy & Environmental Science **7** (2), 804-811 (2014).
28. G. Nolas, D. Morelli and T. M. Tritt, Annual Review of Materials Science **29** (1), 89-116 (1999).
29. X. Shi, W. Zhang, L. Chen and J. Yang, Physical review letters **95** (18), 185503 (2005).
30. B. Sales, D. Mandrus and R. K. Williams, Science **272** (5266), 1325 (1996).
31. Z. Xiong, X. H. Chen, X. Y. Huang, S. Q. Bai and L. D. Chen, Acta Materialia **58** (11), 3995-4002 (2010).
32. H. Li, X. F. Tang, Q. J. Zhang and C. Uher, Applied Physics Letters **94** (10) (2009).
33. C. Uher, Semiconductors and semimetals **69**, 139-253 (2001).
34. S. Bhattacharya, A. Pope, R. Littleton IV, T. M. Tritt, V. Ponnambalam, Y. Xia and S. Poon, Applied Physics Letters **77** (16), 2476-2478 (2000).
35. J. Yang, G. Meisner and L. Chen, Applied physics letters **85**, 1140 (2004).
36. C. Yu, T.-J. Zhu, R.-Z. Shi, Y. Zhang, X.-B. Zhao and J. He, Acta Materialia **57** (9), 2757-2764 (2009).
37. A. Banik, U. S. Shenoy, S. Anand, U. V. Waghmare and K. Biswas, Chemistry of Materials **27** (2), 581-587 (2015).
38. C.-L. Chen, H. Wang, Y.-Y. Chen, T. Day and G. J. Snyder, Journal of Materials Chemistry A **2** (29), 11171-11176 (2014).
39. Y. Chen, M. D. Nielsen, Y. B. Gao, T. J. Zhu, X. Zhao and J. P. Heremans, Advanced Energy Materials **2** (1), 58-62 (2012).
40. E. K. Chere, Q. Zhang, K. Dahal, F. Cao, J. Mao and Z. Ren, Journal of Materials Chemistry A **4** (5), 1848-1854 (2016).
41. Y.-M. Han, J. Zhao, M. Zhou, X.-X. Jiang, H.-Q. Leng and L.-F. Li, Journal of Materials Chemistry A **3** (8), 4555-4559 (2015).
42. Q. Tan, L.-D. Zhao, J.-F. Li, C.-F. Wu, T.-R. Wei, Z.-B. Xing and M. G. Kanatzidis, Journal of Materials Chemistry A **2** (41), 17302-17306 (2014).
43. H. Wu, C. Chang, D. Feng, Y. Xiao, X. Zhang, Y. Pei, L. Zheng, D. Wu, S. Gong, Y. Chen, J. He, M. G.

Inorganic Chemistry Frontiers Accepted Manuscript

Kanatzidis and L.-D. Zhao, Energy Environ. Sci. **8** (11), 3298-3312 (2015).
44. H. Lin, G. Tan, J. N. Shen, S. Hao, L. M. Wu, N. Calta, C. Malliakas, S. Wang, C. Uher and C. Wolverton, Angewandte Chemie International Edition (2016).
45. Y. Tang, R. Hanus, S. Chen and G. Snyder, Nature communications **6**, 7584 (2015).
46. Y. L. Tang, Y. T. Qiu, L. L. Xi, X. Shi, W. Q. Zhang, L. D. Chen, S. M. Tseng, S. W. Chen and G. J. Snyder, Energy & Environmental Science **7** (2), 812-819 (2014).
47. G. J. Tan, Y. Zheng, Y. G. Yan and X. F. Tang, Journal of Alloys and Compounds **584**, 216-221 (2014).
48. G. Tan, S. Wang, X. Tang, H. Li and C. Uher, Journal of Solid State Chemistry **196**, 203-208 (2012).
49. L. W. Fu, J. Y. Yang, J. Y. Peng, Q. H. Jiang, Y. Xiao, Y. B. Luo, D. Zhang, Z. W. Zhou, M. Y. Zhang, Y. D. Cheng and F. Q. Cheng, Journal of Materials Chemistry A **3** (3), 1010-1016 (2015).
50. G. J. Tan, S. Y. Wang, H. Li, Y. G. Yan and X. F. Tang, Journal of Solid State Chemistry **187**, 316-322 (2012).
51. J. Yu, W. Y. Zhao, P. Wei, W. T. Zhu, H. Y. Zhou, Z. Y. Liu, D. G. Tang, B. Lei and Q. J. Zhang, Applied Physics Letters **104** (14) (2014).
52. F. Fahrnbauer, S. Maier, M. Grundei, N. Giesbrecht, M. Nentwig, T. Rosenthal, G. Wagner, G. J. Snyder and O. Oeckler, Journal of Materials Chemistry C **3** (40), 10525-10533 (2015).
53. G. J. Tan, Y. Zheng and X. F. Tang, Applied Physics Letters **103** (18) (2013).
54. G. Rogl, A. Grytsiv, P. Rogl, E. Bauer, M. Hochenhofer, R. Anbalagan, R. C. Mallik and E. Schafler, Acta Materialia **76**, 434-448 (2014).
55. G. J. Tan, W. Liu, H. Chi, X. L. Su, S. Y. Wang, Y. G. Yan, X. F. Tang, W. Wong-Ng and C. Uher, Acta Materialia **61** (20), 7693-7704 (2013).
56. T. Dahal, Q. Jie, G. Joshi, S. Chen, C. F. Guo, Y. C. Lan and Z. F. Ren, Acta Materialia **75**, 316-321 (2014).
57. G. J. Tan, W. Liu, S. Y. Wang, Y. G. Yan, H. Li, X. F. Tang and C. Uher, Journal of Materials Chemistry A **1** (40), 12657-12668 (2013).
58. L. L. Xi, Y. T. Qiu, X. Shi, W. Q. Zhang, L. D. Chen, D. J. Singh and J. H. Yang, Chemical Communications **51** (54), 10823-10826 (2015).
59. Y. L. Li, P. F. Qiu, H. Z. Duan, J. K. Chen, G. J. Snyder, X. Shi, B. B. Iversen and L. D. Chen, Journal of Materials Chemistry C **4** (20), 4374-4379 (2016).
60. G. Rogl, A. Grytsiv, K. Yubuta, S. Puchegger, E. Bauer, C. Raju, R. C. Mallik and P. Rogl, Acta Materialia **95**, 201-211 (2015).
61. G. Rogl, A. Grytsiv, P. Heinrich, E. Bauer, P. Kumar, N. Peranio, O. Eibl, J. Horky, M. Zehetbauer and P. Rogl, Acta Materialia **91**, 227-238 (2015).
62. G. Rogl, A. Grytsiv, P. Rogl, N. Peranio, E. Bauer, M. Zehetbauer and O. Eibl, Acta Materialia **63**, 30-43 (2014).
63. X. Shi, J. Yang, L. Wu, J. R. Salvador, C. Zhang, W. L. Villaire, D. Haddad, J. Yang, Y. Zhu and Q. Li, Scientific Reports **5**, 14641 (2015).
64. D. R. Thompson, C. Liu, J. Yang, J. R. Salvador, D. B. Haddad, N. D. Ellison, R. A. Waldo and J. H. Yang, Acta Materialia **92**, 152-162 (2015).
65. Y. L. Tang, Z. M. Gibbs, L. A. Agapito, G. Li, H. S. Kim, M. B. Nardelli, S. Curtarolo and G. J. Snyder, Nature Materials **14** (12), 1223-1228 (2015).
66. C. Uher, J. Yang, S. Hu, D. Morelli and G. Meisner, Physical Review B **59** (13), 8615 (1999).
67. S. R. Culp, S. J. Poon, N. Hickman, T. M. Tritt and J. Blumm, Applied Physics Letters **88** (4), 1-3 (2006).

Inorganic Chemistry Frontiers Accepted Manuscript

68. Q. Shen, L. Chen, T. Goto, T. Hirai, J. Yang, G. P. Meisner and C. Uher, Applied Physics Letters **79** (25), 4165-4167 (2001).
69. C. G. Fu, T. J. Zhu, Y. T. Liu, H. H. Xie and X. B. Zhao, Energy & Environmental Science **8** (1), 216-220 (2015).
70. S. Chen, K. C. Lukas, W. S. Liu, C. P. Opeil, G. Chen and Z. F. Ren, Advanced Energy Materials **3** (9), 1210-1214 (2013).
71. J. P. A. Makongo, D. K. Misra, X. Y. Zhou, A. Pant, M. R. Shabetai, X. L. Su, C. Uher, K. L. Stokes and P. F. P. Poudeu, Journal of the American Chemical Society **133** (46), 18843-18852 (2011).
72. S. Chen and Z. F. Ren, Materials Today **16** (10), 387-395 (2013).
73. W. J. Xie, A. Weidenkaff, X. F. Tang, Q. J. Zhang, J. Poon and T. M. Tritt, Nanomaterials **2** (4), 379-412 (2012).
74. C. Fu, S. Bai, Y. Liu, Y. Tang, L. Chen, X. Zhao and T. Zhu, Nature Communications **6**, 8144 (2015).
75. A. F. Ioffe, L. S. Stil'Bans, E. K. Iordanishvili, T. S. Stavitskaya and A. Gelbtuch, Physics Today **12** (5), 372-375 (2009).
76. I. B. Cadoff and E. Miller, *Thermoelectric materials and devices*. (Reinhold Pub. Corp.).
77. K. Ahn, M.-K. Han, J. He, J. Androulakis, S. Ballikaya, C. Uher, V. P. Dravid and M. G. Kanatzidis, Journal of the American Chemical Society **132** (14), 5227-5235 (2010).
78. Y. Pei, A. D. LaLonde, N. A. Heinz and G. J. Snyder, Advanced Energy Materials **2** (6), 670-675 (2012).
79. L.-D. Zhao, S. Hao, S.-H. Lo, C.-I. Wu, X. Zhou, Y. Lee, H. Li, K. Biswas, T. P. Hogan, C. Uher, C. Wolverton, V. P. Dravid and M. G. Kanatzidis, Journal of the American Chemical Society **135** (19), 7364-7370 (2013).
80. J. He, S. N. Girard, M. G. Kanatzidis and V. P. Dravid, Advanced Functional Materials **20** (5), 764-772 (2010).
81. J. Androulakis, K. F. Hsu, R. Pcionek, H. Kong, C. Uher, J. J. D'Angelo, A. Downey, T. Hogan and M. G. Kanatzidis, Advanced Materials **18** (9), 1170-1173 (2006).
82. S. Johnsen, J. He, J. Androulakis, V. P. Dravid, I. Todorov, D. Y. Chung and M. G. Kanatzidis, Journal of the American Chemical Society **133** (10), 3460-3470 (2011).
83. G. Tan, F. Shi, S. Hao, L.-D. Zhao, H. Chi, X. Zhang, C. Uher, C. Wolverton, V. P. Dravid and M. G. Kanatzidis, Nat Commun **7**, 12167 (2016).
84. L.-D. Zhao, C. Chang, G. Tan and M. Kanatzidis, Energy & Environmental Science (2016). DOI: 10.1039/C6EE61755J.
85. G. Tan, F. Shi, J. W. Doak, H. Sun, L.-D. Zhao, P. Wang, C. Uher, C. Wolverton, V. P. Dravid and M. G. Kanatzidis, Energy & Environmental Science **8** (1), 267-277 (2015).
86. Q. Zhang, B. Liao, Y. Lan, K. Lukas, W. Liu, K. Esfarjani, C. Opeil, D. Broido, G. Chen and Z. Ren, Proceedings of the National Academy of Sciences **110** (33), 13261-13266 (2013).
87. G. Tan, L.-D. Zhao, F. Shi, J. W. Doak, S.-H. Lo, H. Sun, C. Wolverton, V. P. Dravid, C. Uher and M. G. Kanatzidis, Journal of the American Chemical Society **136** (19), 7006-7017 (2014).
88. L. Aggarwal, A. Banik, S. Anand, U. V. Waghmare, K. Biswas and G. Sheet, Journal of Materiomics **2** (2), 196-202 (2016).
89. K. Chang, J. W. Liu, H. C. Lin, N. Wang, K. Zhao, A. M. Zhang, F. Jin, Y. Zhong, X. P. Hu, W. H. Duan, Q. M. Zhang, L. Fu, Q. K. Xue, X. Chen and S. H. Ji, Science **353** (6296), 274-278 (2016).
90. G. J. Tan, F. Y. Shi, S. Q. Hao, L. D. Zhao, H. Chi, X. M. Zhang, C. Uher, C. Wolverton, V. P. Dravid and M. G. Kanatzidis, Nature Communications **7** (2016).

Inorganic Chemistry Frontiers Accepted Manuscript

91. S. Sakurada and N. Shutoh, Applied Physics Letters **86** (8) (2005).
92. R. Brebrick and A. Strauss, Physical Review **131**, 104-110 (1963).
93. L. Rogers, Journal of Physics D: Applied Physics **1** (7), 845 (1968).
94. A. N. Veis and Y. I. Ukhanov, Soviet Physics Semiconductors-Ussr **10** (7), 780-783 (1976).
95. M. Zhou, Z. M. Gibbs, H. Wang, Y. Han, C. Xin, L. Li and G. J. Snyder, Physical Chemistry Chemical Physics **16** (38), 20741-20748 (2014).
96. V. P. Vedeneev, S. P. Krivoruchko and E. P. Sabo, Semiconductors **32** (3), 241-244 (1998).
97. G. Tan, F. Shi, S. Hao, H. Chi, L. D. Zhao, C. Uher, C. Wolverton, V. P. Dravid and M. G. Kanatzidis, J Am Chem Soc **137** (15), 5100-5112 (2015).
98. G. Tan, F. Shi, S. Hao, H. Chi, T. P. Bailey, L. D. Zhao, C. Uher, C. Wolverton, V. P. Dravid and M. G. Kanatzidis, J Am Chem Soc **137** (35), 11507-11516 (2015).
99. L. D. Zhao, X. Zhang, H. Wu, G. Tan, Y. Pei, Y. Xiao, C. Chang, D. Wu, H. Chi, L. Zheng, S. Gong, C. Uher, J. He and M. G. Kanatzidis, J Am Chem Soc **138** (7), 2366-2373 (2016).
100. J. He, X. Tan, J. Xu, G.-Q. Liu, H. Shao, Y. Fu, X. Wang, Z. Liu, J. Xu, H. Jiang and J. Jiang, J. Mater. Chem. A **3** (39), 19974-19979 (2015).
101. I. U. r. I. Ravich, B. A. e. Efimova and I. A. Smirnov, *Semiconducting lead chalcogenides*. (Plenum Publishing Corporation, 1970).
102. A. Andreev and V. Radionov, Soviet Physics-Semiconductors **1**, 145-148 (1967).
103. R. F. Brebrick and A. J. Strauss, Physical Review **131** (1), 104-& (1963).
104. R. Al Rahal Al Orabi, N. A. Mecholsky, J. Hwang, W. Kim, J.-S. Rhyee, D. Wee and M. Fornari, Chemistry of Materials **28** (1), 376-384 (2016).
105. W. Li, Z. Chen, S. Lin, Y. Chang, B. Ge, Y. Chen and Y. Pei, Journal of Materiomics **1** (4), 307-315 (2015).
106. X. Tan, G. Liu, J. Xu, H. Shao, J. Jiang and H. Jiang, Physical Chemistry Chemical Physics **18** (30), 20635-20639 (2016).
107. Y. Pei, H. Wang and G. J. Snyder, Adv Mater **24** (46), 6125-6135 (2012).
108. S. A. Nemov and Y. I. Ravich, Uspekhi Fizicheskikh Nauk **168** (8), 817-842 (1998).
109. G. S. Bushmarina, B. F. Gruzinov, I. A. Drabkin, E. Y. Lev and V. M. Yuneev, Soviet Physics Semiconductors-Ussr **18** (12), 1374-1377 (1984).
110. M. Zhou, Z. M. Gibbs, H. Wang, Y. Han, L. Li and G. J. Snyder, Applied Physics Letters **109** (4), 042102 (2016).
111. G. Tan, F. Shi, H. Sun, L.-D. Zhao, C. Uher, V. P. Dravid and M. G. Kanatzidis, J. Mater. Chem. A **2** (48), 20849-20854 (2014).
112. G. Tan, W. G. Zeier, F. Shi, P. Wang, G. J. Snyder, V. P. Dravid and M. G. Kanatzidis, Chemistry of Materials **27** (22), 7801-7811 (2015).
113. A. Banik and K. Biswas, Journal of Materials Chemistry A **2** (25), 9620-9625 (2014).
114. T. Chattopadhyay, J. Pannetier and H. G. Vonschnering, Journal of Physics and Chemistry of Solids **47** (9), 879-885 (1986).
115. B.-Z. Sun, Z. Ma, C. He and K. Wu, Rsc Advances **5** (69), 56382-56390 (2015).
116. G. Shi and E. Kioupakis, Journal of Applied Physics **117** (6) (2015).
117. M. Parenteau and C. Carlone, Physical Review B **41** (8), 5227-5234 (1990).
118. J. Vidal, S. Lany, M. d'Avezac, A. Zunger, A. Zakutayev, J. Francis and J. Tate, Applied Physics Letters **100** (3) (2012).
119. A. Ettema, R. A. Degroot, C. Haas and T. S. Turner, Physical Review B **46** (12), 7363-7373 (1992).

Inorganic Chemistry Frontiers Accepted Manuscript

120. L. A. Burton, D. Colombara, R. D. Abellon, F. C. Grozema, L. M. Peter, T. J. Savenije, G. Dennler and A. Walsh, Chemistry of Materials **25** (24), 4908-4916 (2013).
121. F. Ke, J. Yang, C. Liu, Q. Wang, Y. Li, J. Zhang, L. Wu, X. Zhang, Y. Han, B. Wu, Y. Ma and C. Gao, Journal of Physical Chemistry C **117** (12), 6033-6038 (2013).
122. W. Albers, C. Haas and F. Vandermaesen, Journal of Physics and Chemistry of Solids **15** (3-4), 306-310 (1960).
123. C. Guillen, J. Montero and J. Herrero, Physica Status Solidi a-Applications and Materials Science **208** (3), 679-683 (2011).
124. K.-M. Chung, D. Wamwangi, M. Woda, M. Wuttig and W. Bensch, Journal of Applied Physics **103** (8) (2008).
125. J. D. Wasscher, W. Albers and C. Haas, Solid-State Electronics **6** (3), 261-264 (1963).
126. Y. Pei, Z. M. Gibbs, A. Gloskovskii, B. Balke, W. G. Zeier and G. J. Snyder, Advanced Energy Materials **4** (13) (2014).
127. S. J. Silverman and H. Levinstein, Physical Review **94** (4), 871-876 (1954).
128. G. Z. Bagiyeva, N. B. Mustafayev, G. D. Abdinova and D. S. Abdinov, Semiconductors **45** (11), 1391-1394 (2011).
129. J. J. Ning, K. K. Men, G. J. Xiao, B. Zou, L. Wang, Q. Q. Dai, B. B. Liu and G. T. Zou, Crystengcomm **12** (12), 4275-4279 (2010).
130. F. Serrano-Sanchez, M. Gharsallah, N. M. Nemes, F. J. Mompean, J. L. Martinez and J. A. Alonso, Applied Physics Letters **106** (8) (2015).
131. H. Ju and J. Kim, Ceramics International **42** (8), 9550-9556 (2016).
132. S. Sassi, C. Candolfi, J. B. Vaney, V. Ohorodniichuk, P. Masschelein, A. Dauscher and B. Lenoir, Applied Physics Letters **104** (21) (2014).
133. Y. Li, B. He, J. P. Heremans and J.-C. Zhao, Journal of Alloys and Compounds **669**, 224-231 (2016).
134. A. de Kergommeaux, J. Faure-Vincent, A. Pron, R. de Bettignies, B. Malaman and P. Reiss, Journal of the American Chemical Society **134** (28), 11659-11666 (2012).
135. P. Turkes, C. Pluntke and R. Helbig, Journal of Physics C-Solid State Physics **13** (26), 4941-4951 (1980).
136. I. Stambolova, K. Konstantinov, S. Vassilev, P. Peshev and T. Tsacheva, Materials Chemistry and Physics **63** (2), 104-108 (2000).
137. M. Parthibavarman, V. Hariharan and C. Sekar, Materials Science & Engineering C-Materials for Biological Applications **31** (5), 840-844 (2011).
138. H.-Q. Leng, M. Zhou, J. Zhao, Y.-M. Han and L.-F. Li, Rsc Advances **6** (11), 9112-9116 (2016).
139. T.-R. Wei, G. Tan, X. Zhang, C.-F. Wu, J.-F. Li, V. P. Dravid, G. J. Snyder and M. G. Kanatzidis, Journal of the American Chemical Society **138** (28), 8875-8882 (2016).
140. H. Leng, M. Zhou, J. Zhao, Y. Han and L. Li, Journal of Electronic Materials **45** (1), 527-534 (2016).
141. Q. Zhang, E. K. Chere, J. Y. Sun, F. Cao, K. Dahal, S. Chen, G. Chen and Z. F. Ren, Advanced Energy Materials **5** (12) (2015).
142. S. R. Popuri, M. Pollet, R. Decourt, F. D. Morrison, N. S. Bennett and J. W. G. Bos, Journal of Materials Chemistry C **4** (8), 1685-1691 (2016).
143. Y. J. Fu, J. T. Xu, G. Q. Liu, J. K. Yang, X. J. Tan, Z. Liu, H. M. Qin, H. Z. Shao, H. C. Jiang, B. Liang and J. Jiang, Journal of Materials Chemistry C **4** (6), 1201-1207 (2016).
144. J. J. Yan, F. Ke, C. L. Liu, L. Wang, Q. L. Wang, J. K. Zhang, G. H. Li, Y. H. Han, Y. Z. Ma and C. X. Gao, Physical Chemistry Chemical Physics **18** (6), 5012-5018 (2016).

Inorganic Chemistry Frontiers Accepted Manuscript

145. D. Parker and D. J. Singh, Journal of Applied Physics **108** (8) (2010).
146. M. M. Nassary, Journal of Alloys and Compounds **398** (1-2), 21-25 (2005).
147. W. Albers, C. Haas, H. Vink and J. Wasscher, Journal of Applied Physics **32** (10), 2220-2225 (1961).
148. K. T. R. Reddy, N. K. Reddy and R. W. Miles, Solar Energy Materials and Solar Cells **90** (18-19), 3041-3046 (2006).
149. C. Bera, S. Jacob, I. Opahle, N. S. H. Gunda, R. Chmielowski, G. Dennler and G. K. H. Madsen, Physical Chemistry Chemical Physics **16** (37), 19894-19899 (2014).
150. Q. Zhang, E. K. Chere, J. Sun, F. Cao, K. Dahal, S. Chen, G. Chen and Z. Ren, Advanced Energy Materials **5** (12) (2015).

Inorganic Chemistry Frontiers Accepted Manuscript